

# Three-dimensional characterization of extreme ultraviolet mask blank defects by interference contrast photoemission electron microscopy

Jingquan Lin<sup>1,6\*</sup>, Nils Weber<sup>2</sup>, Matthias Escher<sup>2</sup>, Jochen Maul<sup>3</sup>, Hak-Seung Han<sup>4</sup>, Michael Merkel<sup>2</sup>, Stefan Wurm<sup>5</sup>, Gerd Schönhense<sup>3</sup> and Ulf Kleineberg<sup>1</sup>

<sup>1</sup>Faculty of Physics, Ludwig Maximilians University, Munich, D 85748, Germany

<sup>2</sup>Focus GmbH, Huenstetten-Kesselbach, D 65510, Germany

<sup>3</sup>Institute of Physics, Mainz University, Mainz, D 55099, Germany

<sup>4</sup>Samsung Electronics, Photomask Team, Ban-Wol, Hwasung, Kyunggi, Korea 445-701

<sup>5</sup>SEMATECH, 255 Fuller Road, Suite 309, Albany, NY 12203, U.S.A.

<sup>6</sup>Changchun University of Science and Technology, Changchun 130022, China

\*Corresponding author: [Jingquan.lin@physik.uni-muenchen.de](mailto:Jingquan.lin@physik.uni-muenchen.de)

**Abstract:** A photoemission electron microscope based on a new contrast mechanism “interference contrast” is applied to characterize extreme ultraviolet lithography mask blank defects. Inspection results show that positioning of interference destructive condition (node of standing wave field) on surface of multilayer in the local region of a phase defect is necessary to obtain best visibility of the defect on mask blank. A comparative experiment reveals superiority of the interference contrast photoemission electron microscope (Extreme UV illumination) over a topographic contrast one (UV illumination with Hg discharge lamp) in detecting extreme ultraviolet mask blank phase defects. A depth-resolved detection of a mask blank defect, either by measuring anti-node peak shift in the EUV-PEEM image under varying inspection wavelength condition or by counting interference fringes with a fixed illumination wavelength, is discussed.

©2008 Optical Society of America

OCIS codes: (110.0180) Microscopy; (110.5220) Photolithography

---

## References and links

1. K. A. Goldberg, A. Barty, Y. Liu, P. Kearney, Y. Tezuka, T. Terasawa, J. Taylor, H. Han, and O. Wood II, “Actinic inspection of extreme ultraviolet programmed multilayer defects and cross-comparison measurements,” *J. Vac. Sci. Technol.* **B24**, 2824-2828 (2006).
2. T. Liang, P. Sandez, G. Zhang, E. Shu, R. Nagpal, and A. Stivers, “Understand and reduction of defect on finished EUV mask,” *Proc.SPIE* **5752**, 654-662 (2005).
3. Y. Tezuka, M. Ito, T. Terasawa, and T. Tomie, “Actinic detection and signal characterization of multilayer defect on EUV mask blanks,” *Proc.SPIE* **5567**, 791-799 (2004).
4. K. Kinoshita, T. Haga, K. Hanamoto, T. Shohi, M. Endo, and T. Watanabe, “Actinic mask metrology for extreme ultraviolet lithography,” *J. Vac. Sci. Technol. B* **22**, 264-267 (2004).
5. J. Lin, U. Neuhaesler, J. Slieh, and U. Kleineberg “Actinic extreme ultraviolet lithography mask blank defect inspection by photoemission microscopy,” *J. Vac. Sci. Technol.* **B24**, 2631-2635 (2006).
6. V. Farys, P. Schiavone, P. Polack, M. Idir, and V. Muffato, “Highly sensitive detection technology of buried defects in extreme ultraviolet masks using at-wavelength scanning dark-field microscopy,” *Appl. Phys. Lett.* **87**, 024102 (2005).
7. A. Oelsner, O. Schmidt, M. Schicketanz, and G. Schönhense “Microspectroscopy and imaging using a delay line detector in time-of-flight photoemission microscopy,” *Rev. Sci. Instrum.* **72**, 3968-3974 (2001).
8. K. Siegrist, E. Williams, and V. Ballarotto, “Characterizing topography-induced contrast in photoelectron emission microscopy,” *J. Vac. Sci. Technol. A* **21**, 1098-1102 (2003).
9. G. Schönhense, A. Oelsner, and O. Schmidt, “Time-of-flight photoemission electron microscopy—a new way to chemical surface analysis,” *Surf. Sci.* **480**, 180-187 (2001).
10. C. M. Schneider and G. Schönhense, “Investigating surface magnetism by means of photoexcitation electron emission microscopy,” *Rep. Prog. Phys.* **65**, 1785-1839 (2002).
11. G. Schönhense, U. Kleineberg, German patent DE 100 32 979 A1 (Jan.17, 2002).

12. J. Lin, N. Weber, J. Maul, S. Hendel, K. Rott, M. Merkel, G. Schönhense, and U. Kleingerg, "At-wavelength inspection of sub-40nm defects in extreme ultraviolet lithography mask blank by photoemission electron microscopy," *Opt. Lett.* **32**, 1875-1877 (2007).
  13. D. L. Windt, "IMD-Software for modeling the optical properties of multilayer films," *Comput. Phys.* **12** 360-372 (1998).
  14. D. T. Attwood, *Soft X-ray and Extreme Ultraviolet Radiation: Principle and Application* (Cambridge University Press, 2000).
- 

## 1. Introduction

The manufacturing of multilayer coated defect-free mask blanks remains a key challenge for the implementation of extreme ultraviolet lithography (EUVL). Defect inspection of the EUV mask blanks is a metrology key to enabling defect-free mask blanks. Critical defects in EUVL mask blanks include amplitude (absorbing) defects and phase defects. In particular, a tiny bump or pit-type substrate defect, which is buried beneath the multiple layers, primarily affects the phase of the EUV light reflected off the mask and can lead to a printable defect on the wafer. Experiments have shown that phase-type defects are much more difficult to detect than amplitude defects [1]. To achieve the defect requirement for EUV mask blanks of less than 0.003 defects/cm<sup>2</sup> at 25 nm size for the 32 nm half-pitch (hp) node, the industry will require a next generation of mask blank defect inspection tools. Among the candidate technologies that have been investigated so far are various at-wavelength (EUV illumination at 13.5 nm) mask blank inspection methods [2-6] that use EUV imaging techniques to detect defects. Photoemission electron microscopy (PEEM) is a widely used technique for the non-invasive characterization of surfaces with high lateral resolution detection, taking advantage of the photoelectric effect and superior resolution of electron optics. PEEM's elemental selectivity, the capability of spatiotemporal mapping of chemical surface reactions, as well as the element specific imaging of magnetic domains greatly contributes to the popularity of this technique. Depending on the illumination source, different contrast mechanisms can be achieved. Most work done up to now makes use of work function, topographic, chemical and magnetic contrast mechanisms in a PEEM for the investigation of surfaces [7-10]. Different from widely used PEEM contrast mechanisms we investigated PEEM imaging using a new interference contrast mechanism that could be used for at-wavelength EUVL mask blank defect inspection [11]. Previously, it has been shown that the EUV PEEM technique can detect multilayer defects 35 nm wide and 4 nm high [12]. In this article we discuss how this new PEEM image contrast is influenced by the phase of the wave front of the interference field at the mask blank surface as well as the unique role of the interference contrast mechanism in characterizing mask blank defects with respect to their 3-dimensional topography.

## 2. Experiment

The EUV-PEEM microscope used in this experiment is a modified PEEM based on a commercially available system (Focus GmbH, Germany). The sample (EUVL mask blank) is illuminated by EUV light using synchrotron radiation at BESSY II, Berlin at near normal incident angle by inserting a broadband EUVL multilayer coated mirror close to the PEEM diffraction plane as shown in Fig.1.

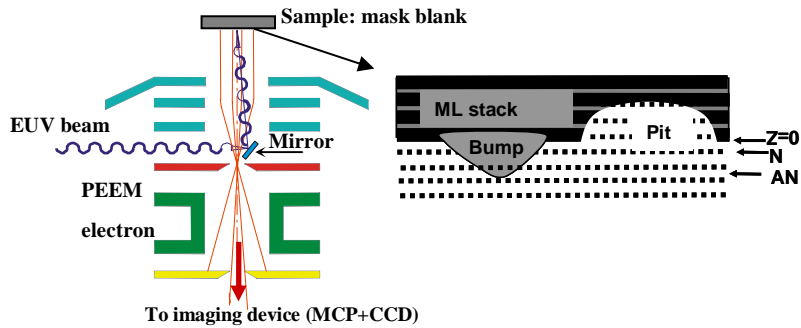


Fig. 1. Illustration of the modified EUV-PEEM. The enlarged diagram of the sample illustrates two types of defects (bump and pit) on top of a multilayer surface in the standing wave field.  $Z=0$  is the position of the mask blank surface. The defect penetrates through node (N) and anti-node (AN) of the field alternatively.

An EUVL mask blank is a distributed Bragg reflector and reflects EUV light at 13.5 nm wavelength. It is made of a stack of  $\sim 40$  pairs of Mo/Si on a glass substrate. Inside the multilayer stack a standing wave field is generated from the superposition of incoming and reflected waves and this field extends many nanometres above the multilayer surface (see enlarged diagram of the sample in Fig. 1). Our simulation of the standing wave field using 40 pairs of Mo/Si bilayers to build the multilayer stack

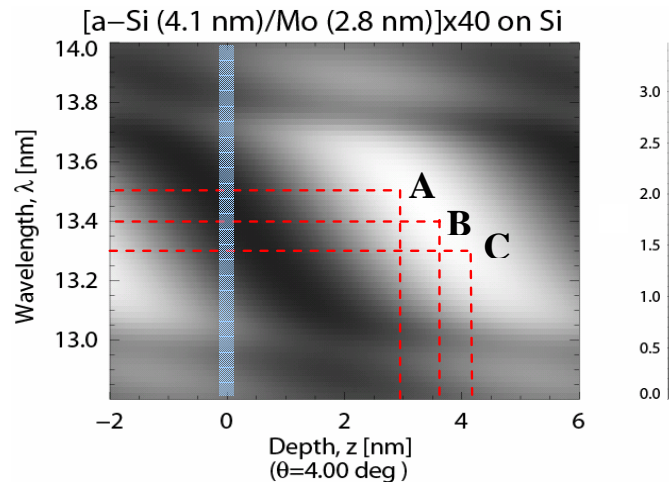


Fig. 2. Calculated electric field contour for a EUVL multilayer stack ( $z=0$  is the position of multilayer surface. For eye guide, multilayer surface is marked by a light blue line in the Fig.2;  $z>0$  ML stack) as a function of wavelength and depth into the multilayer stack at a EUV incident angle of  $4^\circ$  relative to the mask normal using IMD software[13]. The marked dashed red lines are used to indicate spatial shift of the anti-node peak ( $z$  coordinate) induced by a variation of illumination wavelength. A, B and C points correspond to the case of illumination wavelengths of 13.5, 13.4 and 13.3 nm, respectively.

for various wavelengths around the Bragg peak show that the multilayer surface is being penetrated by a wave front node or anti-node depending on the wavelength of the incident radiation around the Bragg peak (Fig. 2). The wavelength-dependent wave-front phase of the standing wave field enables node/anti-node engineering to position at multilayer surface to enhance the local phase shift of the wave front which might originate from substrate defects as

well as irregularities in the multilayer stack, via the emission of secondary electrons and photoelectrons. Contrast of a structure in PEEM image is established through detecting photoemission electron yield variation of the structure region from its surroundings. The PEEM images photoelectrons that are excited by a light source. In the case of EUV is used (so called EUV-PEEM), escape depth of the photoelectron is about 1 nm [14]. Therefore, the intensity of the PEEM image will depend on the electrical field intensity within the first 1 nm beneath the surface. The positioning of a node at the multilayer surface minimizes electron yield (as electron yield is proportional to the local field intensity and this corresponds to a “dark” background in the PEEM image) at the surface and enhances the contrast between a defect and the defect-free multilayer surface. In the case of EUVL multilayer as calculated in Fig.2, when the inspection wavelength is chosen such that a standing wave node appears at the multilayer surface (13.5nm), defects appear bright because they lift the destructive interference condition present in the region of the undisturbed multilayer. Moreover, the interference contrast PEEM simultaneously offers the possibility of a depth-resolved (perpendicular to mask surface) characterization of a defect. The technology is illustrated in the enlarged diagram of the sample shown in Fig. 1. As illustrated in the diagram, a tiny defect (bump/pit) penetrates through a standing wave field generated by the multilayer stack. Node and anti-node of the standing wave field interact through the edges of the defect alternatively as set by the period of the bi-layer pair of Mo/Si (equal to half of the inspection wavelength). An alternation of node (low photoelectron yield) and anti-node (high photoelectron yield) at the edge of the defect results in interference fringes in the PEEM image and the depth of the defect can be determined quantitatively by counting the number of the fringes formed at the edges of the defect.

A mask with programmed pit-type phase defects and an absorbing line structure (the line was etched with a focused ion beam into the multilayer structure) was used to demonstrate how the interference contrast method for EUV-PEEM enhances the visibility of a phase defect. The defect layout on the mask blank is shown in Fig. 3. Isolated substrate pits of 150 nm lateral size and 6 nm depth are arranged in 8x8 arrays with a distance of 10 μm between neighboring defects, (hereinafter called an array pattern) or in varying proximity to the absorbing line (hereinafter called a pit-line pattern) on the sample. 40 Mo/Si bi-layers were deposited on the programmed defect sample using ion beam deposition (IBD). In the pit-line pattern, spacing between pits and edges of the absorbing line varies as shown in Fig. 3. The cross-sectional scanning electron microscope (SEM) image of the line in Fig. 3 shows that it was created with multilayer slopes on both sides. The pit-line pattern is designed to test pit defects printability.

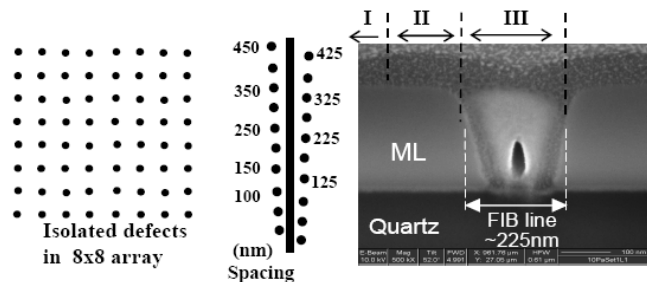


Fig. 3. Phase defects layout in the array with spacing of ~10 μm (left), or in pit-line pattern (middle) with varying proximity to the line (the dark dots around the line represent pit defects with varying distance to edge of the line as marked in the sketch). Image (right) is a cross sectional SEM photo of the absorbing line. I, II and III mark the defect-free multilayer, multilayer slope and absorbing zone, respectively. The grainy structure on top of multilayer is the deposited gold material for a purpose of obtaining SEM image of the multilayer structure. The dark dot in the middle of the image is void formed during the gold deposition.

### 3. Results and discussions

Figure 4(a) shows EUV-PEEM images of the isolated 150 nm (w)/6 nm (h) pit-type phase defects in the 8x8 array pattern, displayed in a quite large field of view (FoV  $\sim 70 \mu\text{m}$ ). As can be seen from the image, defects located in FoV of the PEEM are all clearly observed. In order to correct the image for inhomogeneous sample illumination we performed a flat-field correction in this image by subtracting two PEEM images with the same microscope settings. The sample was slightly shifted for the second image. This procedure results in a “double image”, showing the defects as bright as well as dark spots in the PEEM image. Figure 4(b) shows EUV-PEEM images obtained from the pit-line pattern area at various inspection wavelengths, which are mainly used to show the same size pit defects placed near the line at different proximity as defined in Fig. 3. The central wavelength-independent bright lines in PEEM images represent the absorbing structures, and the bright/dark edges (depending on inspection wavelength) surrounding the line correspond to the multilayer slopes. Two dot-shaped structures that appear in the center of each PEEM images are alignment markers with much larger size. Insets in each PEEM image show line-scan intensity profiles of the defect areas extracted along the lower dark/bright edge (position and direction of the line-scan is marked with a black arrow in Fig. 4(b) at 13.5 nm). The clearly-observed minimal phase defect size is about 150nm(w)/6nm(h) in this inspection, which is much larger than PEEM’s spatial resolution (50-100nm) at the operational mode of EUV illumination. This is because the currently-employed 6 inch size sample holder and the corresponding x-y-z control stage was not integrated with PEEM’s electronic optics part as our previous measurements did, but fixed on top of the vacuum chamber. Vibration of the stage limits minimum of the detectable defect size in this particular measurement. A striking feature of the PEEM image is that the visibility of these tiny pit defects is strongly wavelength-dependent. For example, the defects near the absorbing line are clearly observed at wavelength of 13.1nm (as marked from 1 to 5 in this PEEM image) rather than other wavelengths, and accordingly it shows five peaks in the line-scan profile. We also noted that best visibility of the defects in the array and pit-line pattern corresponds to different inspection wavelengths (best visibility of the defects in the array region is at 13.5 nm as shown in Fig.4(a); PEEM images at other wavelengths for this region are not given here).

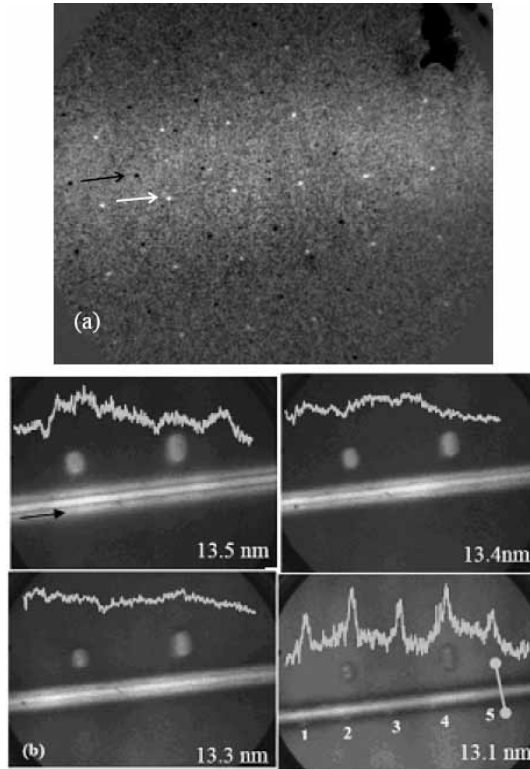


Fig. 4. EUV-PEEM image of pit-type defects in (a) the array pattern (FoV~70 $\mu$ m, backfield corrected) at inspection wavelength of 13.5nm and (b) pit-line pattern (FoV~12 $\mu$ m) at 13.5 nm to 13.1nm. To guide the eye, a white and a black arrows are used to align one of the lines of the black and white dots array in Fig. 4(a) respectively, the pit defects closest to the line in (b) are marked with #1,2,3,4 and 5, and line-scan profiles of the defects are given in the inset. The defects have a distance of 300 (#1), 250, 200 150 100 (#5) nm from the edge of the line, respectively. The two markers in the image center have sizes of 300 (w) x 10 (h) nm (left marker) and 500 (w) x 10 (h) nm (right marker), respectively.

The wavelength-dependent visibility of phase defects can be explained by the interference contrast of the EUV-PEEM. Figure 5 shows typical line-scan intensity profiles from the PEEM image of Fig. 4(b) extracted perpendicularly across the line as well as the multilayer slopes and defect-free region (scanning position is indicated by the straight line with ending points in Fig. 4(b) at 13.1 nm) at wavelengths around the Bragg peak. In a PEEM image, the brightness in a given area is proportional to the intensity of electron emission from that area. There is a large variation in electron yield (as indicated by the CCD count in Fig. 5) of the defect-free multilayer region as well as the multilayer slopes in the PEEM image when changing inspection wavelength. The electron yield at the defect-free multilayer surface in the PEEM image varies from low to high by tuning the wavelength from 13.5 nm to 13.1 nm, which indicates that the wave-front of the standing wave field at the multilayer surface is shifting from node to anti-node as the wavelengths is shifted. The observed electron yield variation versus incident wavelength is in agreement with the electric field intensity simulation results at the multilayer surface shown in Fig. 2. However, as shown in Fig. 5, the electron yield variation trend at the multilayer slopes is inverted to that of the defect-free multilayer area. For example, the slope region shows low electron yield at a wavelength of 13.1 nm. This indicates that the wave-front of the standing wave in the slope region is in node locally at this wavelength. The observation of a 180° phase shift of the wave-front on the

slopes with respect to the defect-free multilayer surface at a given wavelength is due to the reduced multilayer stack height at the slope. This phase shift causes the best visibility of pit defects in the array and pit-line pattern corresponds to different wavelengths. For example, the best visibility of defects in the array is found at 13.5nm, appearing as node of standing wave located at defect-free multilayer surface (surrounding of defects in the array pattern). On the other hand, the best visibility of defects in the pit-line region is found at 13.1nm, which corresponds to anti-node located at defect-free multilayer surface. However, due to 180° phase shift of the wave front at slope with respect to the defect-free multilayer surface, this brings node appearing at the slope region (surrounding of defects in the pit-line pattern) at this wavelength. Consistently, the best visibility of pit defects on the mask blank sample (both in the array and in the pit-line pattern) is obtained at a condition where a standing wave node appears at the local defect position providing the best illumination with minimal electron yield from the defect free surrounding multilayer surface.

The dominating role of the interference contrast in identifying the buried shallow pit defects on the mask blank sample was further demonstrated by use of illumination wavelength of ~248 nm (with Hg discharge source): none of the pit defects (150 nm (w) /6 nm (h)) on the mask blank are visible in the UV-PEEM image. Different from other mask blank defect inspection methods such as dark field microscopy which detects phase defects by measuring scattering light signal induced by a defect [3,6], where a shorter inspection wavelength gives a much higher detection sensitivity on defect size. In the PEEM method, we detect defects by imaging photoemission electrons, in which electron energy distribution width is one of the major determining factors to the achievable spatial resolution of the PEEM. With UV-illumination (248 nm), distribution width of the photoemission electron energy is much narrower (thus with a smaller chromatism similar to the case of an optical microscope) than that obtained with an EUV illumination (13.5 nm). Therefore, in term of illumination wavelength of a PEEM, UV-illumination should offer a better spatial resolution than the case of an EUV illumination. The disappearance of the tiny pit defects in the UV-PEEM image are mainly because there is no interference contrast under this experimental condition, since the illumination wavelength (248 nm) is far away from the resonant wavelength of the multilayer Bragg reflector (13.5nm). Without a standing wave field with a periodicity given by the multilayer stack no modulation of the electron yield with the electric field variation can be observed. Under UV-illumination, the applicable contrast mechanism is judged to be topographic only in this case. The remaining contrast mechanisms such as work function or chemical contrast can be excluded because the multilayer surface is capped by silicon dioxide. The shallow substrate defect-induced topographic contrast is too weak in this case to generate pronounced contrast in the PEEM image. The UV illumination inspection confirms that interference contrast PEEM is much more sensitive in capturing tiny mask blank phase defects than the topographic contrast in PEEM.

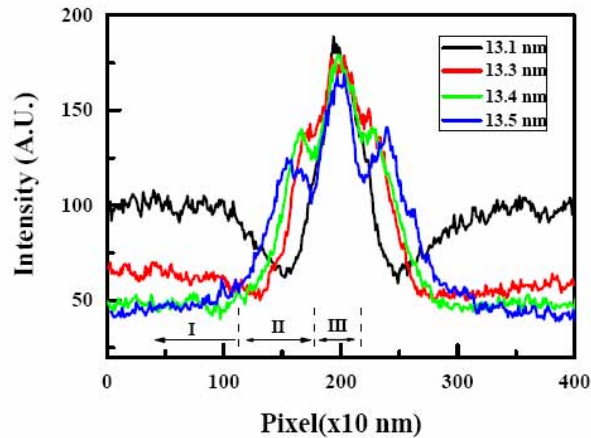


Fig. 5. A typical line-scan profile across defect-free multilayer surface (marked as I), multilayer slope (II) as well as the absorbing line (III). The scanning position is indicated by the line with ending points as shown in Fig.4 (b).

Further analysis of PEEM images at various inspection wavelengths around the Bragg peak of the multilayer can provide depth information of such nanosized structures on mask blanks. It is interesting to note that in Fig. 5 both side peaks (corresponding to the bright edges in the PEEM image induced by anti-nodes of the standing wave) sitting left and right from the central peak (absorbing line) shift towards the central as the illumination wavelength decreases from 13.5 nm to 13.3 nm. This is because the position of the anti-node peaks falls vertically along the multilayer slope as the illumination wavelength decreases (refer to Fig. 2). Based on the anti-node peak shift with wavelength at the multilayer slope in the PEEM images as well as the corresponding anti-node depth variation induced by the wavelength variation as given in Fig. 2, one can estimate the angle of the local multilayer slope. The distance between two neighboring pit defects in Fig. 4 is known to be 2  $\mu\text{m}$  from the sample fabrication process and this distance corresponds to a pixel number of about 200 in the PEEM image. Therefore, using this calibration, the obtained pixel resolution is determined to be  $\sim 10$  nm per pixel. According to Fig. 5, the amount of lateral shift of the anti-node peak in the PEEM images is measured  $\sim (100 \pm 10)$  nm (shift from pixel 155 to 165 in Fig. 5) by tuning the wavelength from 13.5 nm to 13.4 nm. Correspondingly, it follows from the electric field simulation that the anti-node peak depth variation is about 0.75 nm (shifting from A to B point in Fig. 2). Therefore, the angle of the local multilayer slope is estimated to be about  $(0.43 \pm 0.04)^\circ$ . By further reducing the wavelength with another step to 13.3 nm (from B to C point in Fig. 2), the lateral shift of the anti-node peak in the PEEM image decreases from the above of  $\sim 100$  to  $\sim (30 \pm 10)$  nm (shift from pixel 165 to 168 in Fig. 5), which translates into a side wall angle of  $(1.5 \pm 0.5)^\circ$  of the local multilayer slope. The analysis of the opposite side slope with respect to the absorbing line gives a similar result as obtained above. As the wavelength is decreased further the calculated angle of the local multilayer side wall slope steepens. This is in agreement with the fact that the multilayer slope becomes much steeper as it extends toward the central absorbing line. At a wavelength of 13.1 nm the anti-node peak has shifted to a much deeper region of the multilayer slope and is closer to the central absorbing line. There it becomes difficult to resolve the anti-node peaks in the PEEM image due to the resolution limitation of the currently employed PEEM (50 to 100 nm in the operation mode of EUV illumination). Meanwhile, the neighboring node of the standing wave field follows the anti-node peak, shifting to the position that was previously occupied by this anti-node as Fig. 5 shows.

The above analysis shows that the EUV-PEEM technology offers an effective way to determine the angle of the local multilayer slope through measuring spatial shifts of single interference fringe peaks (anti-node/node peak) along the slope in the PEEM image as induced by wavelength variation. In this operation mode, the lateral detection limit for a fringe peak shift can be as low as  $\sim 10$  nm in the PEEM image, and tunable anti-node depth variation can be  $\sim 2.5$  nm as can be seen from Fig. 2 (this corresponds to the case of wavelength variation from 13.6 nm to 13.1 nm within the bandwidth of the multilayer Bragg peak). Therefore local multilayer side wall slopes as steep as  $\sim 14^\circ$  can be measured.

In a different operation mode, where the wavelength is kept constant the technology could be employed to determine height variation of defects by counting the number of interference fringes generated by the anti-node and node interaction on its edges. The EUV-PEEM image in Fig. 6 shows an example of how to use this operational mode to detect a defect while simultaneously capturing depth-resolving information. This PEEM image was obtained from another multilayer defect sample that was prepared using a different fabrication procedure. First, some  $\sim 50$  nm diameter Si balls were sprayed on a silicon wafer surface and then subsequently coated with an EUVL multilayer. The node of the standing wave is intentionally positioned at the defect-free multilayer surface (bottom-left part of the PEEM images) by choosing the resonant wavelength of the multilayer structure. One major feature of the image in Fig. 6 is that interference fringes are observed in the PEEM image, roughly starting from the center of the image and going towards the top-right direction.

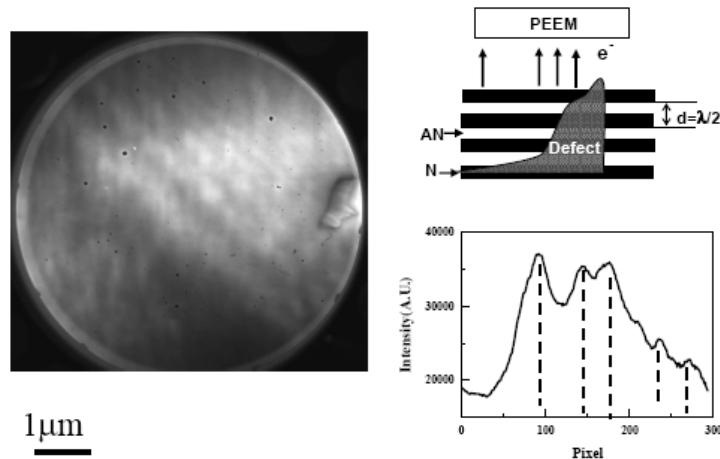


Fig. 6. "Tomographic" EUV-PEEM image obtained with an EUVL mask blank stack at 13.5 nm. The curve is a line-scan profile averaged over five different lines scanned perpendicularly across the fringes. The bright region above the image center is caused by an inhomogeneous EUV illumination. The diagram in the upper right of the figure illustrates one case of edge variation of a defect in the standing wave field (AN: anti-node, N: node). Another defect appears close to the right edge of the PEEM image.

The appearance of interference fringes in the PEEM image is attributed to the existence of a defect on the EUVL mask blank (most probably a slow-varying multilayer slope induced by a section of Si film of unequal height formed through binding of the nanoscale Si balls). The defect's height variation introduces nodes and anti-nodes of standing wave interactions on the slope alternately, thus producing the interference fringes in the PEEM image. Moreover, 5 pairs of fringes can be observed in the PEEM images which are also visible in the line-scan profile made across the fringes in the PEEM image where fringe pairs are indicated with dashed lines. Therefore the measured height variation of the defect shown in this PEEM image is estimated to be  $\sim 35$  nm ( $= 5$  times  $d$ , where  $d$  is half of the inspection wavelength  $\lambda$ ). Furthermore, when checking the image as well as the respective linescan profile carefully, one notices that the period of the interference fringes is not uniform,

showing a decrease as the scan position moves to the top right. A reduction of the interference fringe period is most probably due to a stronger variation of the defect's height as it extends along this direction. This is illustrated by the diagram in Fig. 6, which shows a defect in the standing wave field. It can be directly seen from the diagram how a steeper slope of the defect in the standing wave field translates into a smaller period of interference fringes in the PEEM image.

#### **4. Summary**

The experimental results in this paper show that interference contrast plays a key role in identifying very tiny phase defects when using EUV-PEEM to inspect an EUVL mask blank. The dominating role of the interference contrast in capturing the tiny phase defects is further demonstrated by a comparative measurement of the sample with UV and EUV illumination in the PEEM. In general, PEEM gives a direct measure of the lateral dimensions of the nanostructure on a surface but it does not bear any quantitative information about the height modulation of the structure. Additional characterization is therefore required to determine the height of a structure. However, if assisted by an interference contrast mechanism, as in the case of inspecting EUV mask blanks, the EUV-PEEM offers the capability of sampling the 3-dimensional topography of EUVL mask defects. "Tomographic" PEEM avoids the need to remove the mask blank from the well-defined environment for ex situ analysis. One limitation of the technology is that an abrupt step-shape defect cannot be easily detected with depth-resolved information in the EUV-PEEM image, even though its edge vertically experiences an alternative field intensity interaction of the standing wave field. The determination of a defect's depth information in the EUV-PEEM image largely depends on the spatial resolution of the PEEM instrument. By introducing aberration corrections and energy filters in the PEEM, the lateral resolution of the currently-employed PEEM can be further significantly improved. This should provide additional potential for characterizing the 3D topography of defects with much steeper sloped edges.

#### **Acknowledgments**

We are grateful to BESSY II, Berlin, Germany for the technical support. Help from K. Goldberg at Lawrence Berkeley National Laboratory, Berkeley, California is greatly appreciated.